

# Initial performance of the COSINE-100 experiment

G. Adhikari<sup>1</sup>, P. Adhikari<sup>1</sup>, E. Barbosa de Souza<sup>2</sup>, N. Carlin<sup>3</sup>, S. Choi<sup>4</sup>, W. Q. Choi<sup>5,15</sup>, M. Djamal<sup>6</sup>, A. C. Ezeribe<sup>7</sup>, C. Ha<sup>8,a</sup>, I. S. Hahn<sup>9</sup>, A. J. F. Hubbard<sup>2,16</sup>, E. J. Jeon<sup>8</sup>, J. H. Jo<sup>2</sup>, H. W. Joo<sup>4</sup>, W. G. Kang<sup>8</sup>, W. Kang<sup>10</sup>, M. Kauer<sup>11</sup>, B. H. Kim<sup>8</sup>, H. Kim<sup>8</sup>, H. J. Kim<sup>12</sup>, K. W. Kim<sup>8</sup>, M. C. Kim<sup>10,17</sup>, N. Y. Kim<sup>8</sup>, S. K. Kim<sup>4</sup>, Y. D. Kim<sup>1,8</sup>, Y. H. Kim<sup>8,13</sup>, V. A. Kudryavtsev<sup>7</sup>, H. S. Lee<sup>8</sup>, J. Lee<sup>8</sup>, J. Y. Lee<sup>12</sup>, M. H. Lee<sup>8</sup>, D. S. Leonard<sup>8</sup>, K. E. Lim<sup>2</sup>, W. A. Lynch<sup>7</sup>, R. H. Maruyama<sup>2</sup>, F. Mouton<sup>7</sup>, S. L. Olsen<sup>8</sup>, H. K. Park<sup>8</sup>, H. S. Park<sup>13</sup>, J. S. Park<sup>8,18</sup>, K. S. Park<sup>8</sup>, W. Pettus<sup>2,19</sup>, Z. P. Pierpoint<sup>2</sup>, H. Prihtiadi<sup>6</sup>, S. Ra<sup>8</sup>, F. R. Rogers<sup>2,20</sup>, C. Rott<sup>10</sup>, A. Scarff<sup>7,21</sup>, N. J. C. Spooner<sup>7</sup>, W. G. Thompson<sup>2</sup>, L. Yang<sup>14</sup>, S. H. Yong<sup>8</sup>

<sup>1</sup> Department of Physics, Sejong University, Seoul 05006, Republic of Korea

<sup>2</sup> Department of Physics, Yale University, New Haven, CT 06520, USA

<sup>3</sup> Physics Institute, University of São Paulo, São Paulo 05508-090, Brazil

<sup>4</sup> Department of Physics and Astronomy, Seoul National University, Seoul 08826, Republic of Korea

<sup>5</sup> Korea Institute of Science and Technology Information, Daejeon 34141, Republic of Korea

<sup>6</sup> Department of Physics, Bandung Institute of Technology, Bandung 40132, Indonesia

<sup>7</sup> Department of Physics and Astronomy, University of Sheffield, Sheffield S3 7RH, UK

<sup>8</sup> Center for Underground Physics, Institute for Basic Science (IBS), Daejeon 34047, Republic of Korea

<sup>9</sup> Department of Science Education, Ewha Womans University, Seoul 03760, Republic of Korea

<sup>10</sup> Department of Physics, Sungkyunkwan University, Seoul 16419, Republic of Korea

<sup>11</sup> Department of Physics and Wisconsin IceCube Particle Astrophysics Center, University of Wisconsin-Madison, Madison, WI 53706, USA

<sup>12</sup> Department of Physics, Kyungpook National University, Daegu 41566, Republic of Korea

<sup>13</sup> Korea Research Institute of Standards and Science, Daejeon 34113, Republic of Korea

<sup>14</sup> Department of Physics, University of Illinois at Urbana-Champaign, Urbana, IL 61801, USA

<sup>15</sup> *Present address:* Institut für Experimentelle Kernphysik, Karlsruher Institut für Technologie (KIT), 76344 Eggenstein-Leopoldshafen, Germany

<sup>16</sup> *Present address:* Department of Physics and Astronomy, Northwestern University, Evanston, IL 60208, USA

<sup>17</sup> *Present address:* Department of Physics, Chiba University, Chiba 263-8522, Japan

<sup>18</sup> *Present address:* High Energy Accelerator Research Organization (KEK), Ibaraki 319-1106, Japan

<sup>19</sup> *Present address:* Department of Physics, Center for Experimental Nuclear Physics and Astrophysics, University of Washington, Seattle, WA 98195, USA

<sup>20</sup> *Present address:* Department of Physics, Massachusetts Institute of Technology, Cambridge, MA 02139, USA

<sup>21</sup> *Present address:* Department of Physics and Astronomy, University of British Columbia, Vancouver, BC V6T 1Z1, Canada

Received: 30 November 2017 / Accepted: 25 January 2018

© The Author(s) 2018. This article is an open access publication

**Abstract** COSINE is a dark matter search experiment based on an array of low background NaI(Tl) crystals located at the Yangyang underground laboratory. The assembly of COSINE-100 was completed in the summer of 2016 and the detector is currently collecting physics quality data aimed at reproducing the DAMA/LIBRA experiment that reported an annual modulation signal. Stable operation has been achieved and will continue for at least 2 years. Here, we describe the design of COSINE-100, including the shielding arrangement, the configuration of the NaI(Tl) crystal detection elements, the veto systems, and the associated operational systems, and we show the current performance of the experiment.

## 1 Introduction

Although dark matter appears to be ubiquitous, little is known about it. Numerous astronomical observations, including the velocities of stars and galaxies, anisotropies in the cosmic microwave background, and gravitational lensing measurements have indicated that about 27% of the Universe is comprised of dark matter [1–3]. Theoretical physicists have proposed a weakly interacting massive particle (WIMP) as a particle candidate for the dark matter [4, 5]. They have suggested that rarely occurring interactions between WIMPs in the Milky Way’s dark matter halo and nuclei of normal matter may be measurable with a low-radioactivity detector in a deep underground laboratory [6].

<sup>a</sup> e-mail: [changhyon.ha@gmail.com](mailto:changhyon.ha@gmail.com)

One WIMP signature would be a modulation in the nuclear recoil event rate as an Earth-bound detector sweeps through the galaxy's dark matter halo [7,8]. In a series of measurements that started in 1995, the DAMA/NaI and DAMA/LIBRA experiments (DAMA for short) searched for evidence of an annual modulation signature in an array of low-background NaI(Tl) crystals [9]. Throughout this search, the DAMA group has consistently reported a positive annual modulation signal with a phase consistent with expectations for the Earth's motion relative to the galactic rest frame [10,11]. Their most recent result, based on a 1.33 ton year data with a  $1 \text{ count/day/kg/keV}^1$  background level crystal array, is a  $9.3\sigma$  modulation in the single-site distribution of events in the 2–6 keV range with an amplitude of  $0.0112 \pm 0.0012 \text{ count/day/kg/keV}$ , a phase of  $144 \pm 7$  days and a period of  $0.998 \pm 0.002$  years.

The DAMA signal and, in particular, its interpretation as being due to WIMP-nucleon scattering, is a subject of continuing debate [8,10,12–15]. This is primarily because WIMP-nucleon cross sections inferred from the DAMA modulation in the context of the standard galactic WIMP halo model [8] are in conflict with upper limits from other experiments that are based on time-integrated measurements of the total rate of nuclear recoils, such as LUX [16], PandaX [17,18], XENON [19,20], SuperCDMS [21–23] and KIMS [24]. In addition, XMASS [25] and XENON [26] have reported that their annual modulation measurements based on leptophilic models are inconsistent with DAMA's results. However, no independent experimental confirmation of the DAMA signal with the same target material and the same method has been performed to date.

The dark matter search region of interest corresponds to electron-equivalent nuclear recoil energies below 10 keV. In this energy region, the major internal background contributions in NaI(Tl) crystals are  $^{210}\text{Pb}$   $\beta$  decays with  $Q_\beta = 63.5 \text{ keV}$ ,  $\sim 3 \text{ keV}$  emissions from  $^{40}\text{K}$  decays, and low energy emissions from cosmogenically induced radioisotopes, including  $\sim 3 \text{ keV}$  events from  $^{109}\text{Cd}$ ,  $\sim 4 \text{ keV}$  events from Te/I, and  $^3\text{H}$  beta decays [9,27–29]. The  $^{210}\text{Pb}$  contamination consists of a bulk contamination that is primarily due to impurities in the raw materials used to produce the crystals and surface contamination introduced by exposure to atmospheric  $^{222}\text{Rn}$  during crystal production and handling. The bulk component of  $^{210}\text{Pb}$  ( $T_{1/2} = 22.2 \text{ year}$ ) is difficult to remove from the raw material by commonly used purification methods. The  $\sim 3 \text{ keV}$  K-shell X-rays and Auger electrons from  $^{40}\text{K}$  are mainly produced in the 10.55% of the decays that proceed via electron capture to  $^{40}\text{Ar}$  with the emission of an accompanying 1460 keV  $\gamma$ -ray. The chemical similarity with sodium complicates the removal of potassium contamination from the NaI powder used for the crystal growing.

<sup>1</sup> keV is electron equivalent energy.

One reason for the lack of verification of the DAMA result is that a new NaI(Tl) WIMP search would require an independent development of low-background crystals. The crystal-growing company that supplied the DAMA NaI(Tl) crystals no longer produces similar-grade crystals. Several groups including ANAIS [30,31], DM-Ice [32,33], KamLAND-PICO [34], SABRE [35], and KIMS [27,36], have worked to develop low-background NaI(Tl) crystals suitable for reproducing the DAMA experiment.

Among these groups, KIMS and DM-Ice have joined to construct and operate a single experiment, named COSINE, at the Yangyang underground laboratory (Y2L) in Korea. KIMS and DM-Ice have assembled an eight element, 106 kg array of low-background NaI(Tl) crystals that is currently being used in the COSINE-100 experiment. The construction and assembly of the COSINE-100 detector at Y2L took place in early 2016, and the physics run started in late September of 2016.

This paper is organized as follows: Sect. 2 describes the experimental area and the detector room; Sect. 3 discusses the shielding arrangement; Sect. 4 gives details about the internal radioactivity levels of the individual crystals and describes how they are assembled into the detector array; Sect. 5 provides details about the liquid scintillator veto system, including results from prototype tests; Sect. 6 provides an overview of the cosmic-ray muon tagging system; Sect. 7 gives a brief overview of the data acquisition system; Sect. 8 describes the environmental monitoring system; Sect. 9 reports on the performance levels of the detector system and quality of the initial physics data; Sect. 10 provides descriptions of simulations; Sect. 11 describes the expected sensitivity of COSINE-100 measurements; and Sect. 12 contains concluding remarks and comments.

## 2 Experimental hall

### 2.1 Experimental site at the Yangyang underground laboratory

The COSINE experiment is located in a recently established experimental area in the Y2L A5 tunnel. The Y2L facility is situated next to the underground generators of the Yangyang pumped-storage hydroelectric power plant under Mount Jumbong, 150 km east of Seoul in Korea ( $38^\circ 01' 09.1''\text{N}$ ,  $128^\circ 29' 58.6''\text{E}$ ). The laboratory consists of experimental areas located in the A5 and A6 tunnels and are accessible by car via a 2 km horizontal access tunnel. The experimental areas have a minimum granite overburden of 700 m: the cosmic-ray flux in A5 is measured to be  $3.80 \pm 0.01(\text{stat.}) \pm 0.12(\text{syst.}) \times 10^{-7} \text{ cm}^{-2}\text{s}^{-1}$  [37] while the flux in A6 is  $2.7 \times 10^{-7} \text{ cm}^{-2}\text{s}^{-1}$  [38]. Experimental

rooms are built in the caverns located at the mid-sections of the tunnels. Automatically regulated electrical power, conditioned by uninterruptible supplies, is provided to both experimental areas, with voltages that are continuously monitored. Fresh air from the surface is drawn into the tunnels through the driveways and exhausted via a separate duct. Throughout the year, the A5 tunnel temperature is maintained between 22 and 25 °C and the relative humidity near the laboratory rooms is measured to be in the 60–70% range.

The Korea Invisible Mass Search (KIMS) experiment [24], which operated a CsI(Tl) array for dark matter searches in the A6 area for more than 15 years, has been discontinued and its shielding arrangement refurbished to host a variety of measurements as part of R&D activities related to the development of low background detectors.

## 2.2 Detector room

COSINE-100 is located inside an environmentally controlled room with regulated humidity and temperature, radon-reduced air, and gas supply systems that are monitored remotely online and in the surface-level control room. The

detector room is 44 m<sup>2</sup> in area and 4 m high, and is maintained as an access-controlled clean air environment. In order to minimize contact with the air in the tunnel, which contains  $1.20 \pm 0.49$  pCi/L of <sup>222</sup>Rn and other background components [39], the room atmosphere is isolated from that of the tunnel. The room air is continuously circulated through a HEPA filter and the maximum number of dust particles larger than 0.5 μm is kept below 1500 per cubic foot. During detector installation periods, radon-reduced air, with a contamination that is a factor of 100 below the tunnel atmosphere level, is provided to the room. The air control system maintains the room temperature at  $(23.5 \pm 0.3)$  °C and the relative humidity at  $(40 \pm 3)$  %.

## 3 Main shielding structure

The COSINE shielding structure inherited many features from KIMS [40,41] and was designed to attenuate or tag the influence of external sources of radiation as efficiently as possible. The detector is contained in a 4-layer nested arrangement of shielding components as shown in Fig. 1. It

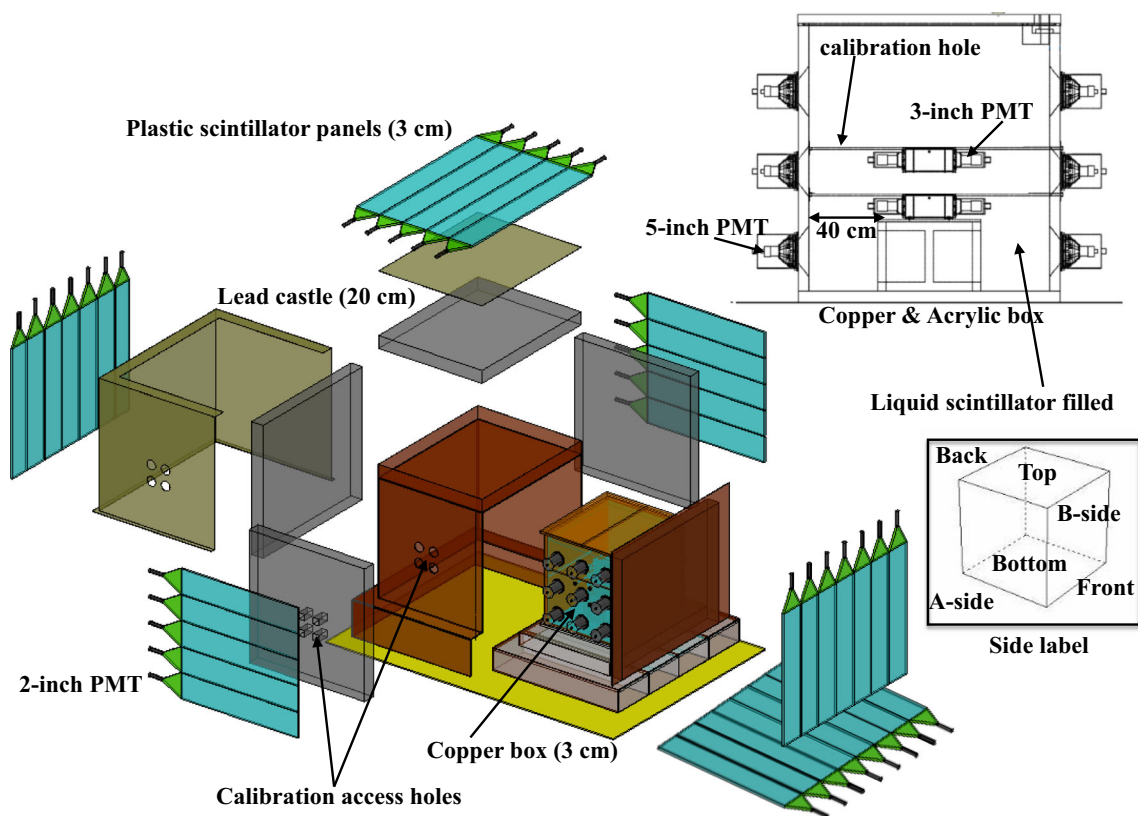


**Fig. 1** COSINE shielding overview. From outside inward, muon panels (3 cm thick, light blue), a lead brick castle (20 cm thick on all sides, grey), a copper box (3 cm thick), an acrylic box (1 cm thick) and eight encapsulated crystal detectors immersed in the liquid scintillator

(> 40 cm from crystal assembly to wall on all sides) are shown. Also indicated are the locations of the calibration holes, the size of the PMTs, and labeling scheme for the different sides. Here, the lead shields at the bottom and the front side are omitted for clarity



**Fig. 2** Photo of the COSINE detector with the front side open. Plastic scintillators with black covers and an orange copper box with 5-inch PMT assemblies are shown. A hoist is used to move the 800 kg top cover of the copper box

provides  $4\pi$  coverage against external radiation from various sources. The shield is supported by a steel skeleton<sup>2</sup> that surrounds a 300 cm (L)  $\times$  220 cm (W)  $\times$  270 cm (H) volume. From outside inward, the four shielding layers are plastic scintillator panels, a lead-brick castle, a copper box, and a scintillating liquid, as described below. The eight NaI(Tl) crystal assemblies and their support table are immersed in the scintillating liquid. The front side of the shield rests on a linear rail and can slide open at a speed of 40 cm per minute. A photograph of the detector with the front side open is shown in Fig. 2.

### 3.1 Plastic scintillator panels

An array of plastic scintillation counters provides a simple and reliable method for tagging cosmic-ray muons that pass through or near the detector. The array of plastic scintillator panels that surrounds the COSINE detector records and flags cosmic-ray muons and muon-induced events in the same data stream as the crystal data. The main purpose of this system is to enable studies of correlations between cosmic-ray muons and crystal signals, as high-energy muons are known to affect the response of NaI(Tl) crystals over a time interval that extends beyond the 8  $\mu$ s window of the crystal readout system [12, 42]. Additionally, coincidence rates between different panels in the system can be used to infer the cosmic-ray muon flux.

### 3.2 Lead castle

A 20 cm-thick lead castle that surrounds the copper box attenuates  $\gamma$ -rays that originate from outside the shielding structure. The inner half of this shield is made of low-contamination lead that contains  $^{238}\text{U}$  and  $^{232}\text{Th}$  concen-

trations of 6.9 and 3.8 ppt, respectively. The  $^{210}\text{Pb}$  content was measured to be  $30 \pm 1$  Bq/kg at Y2L using alpha counting of  $^{210}\text{Po}$  decay while the supplier's specification shows  $59 \pm 6$  Bq/kg using  $^{210}\text{Bi}$  beta counting. The discrepancy is mainly due to different treatment of sample's surface emission. The outer half of the shield is made of normal lead with 99.99% purity. The lead is in the form of 20 cm  $\times$  10 cm  $\times$  5 cm rectangular bricks stacked in such a way that there is no open channel between the outer and inner layers. The total weight of the lead shield is 56 tons. The bricks were cleaned with ethanol prior to installation.

### 3.3 Copper box

The copper box serves as a shield for  $\gamma$ -rays as well as a support for the liquid scintillator. ICP-MS measurements of the copper were 27 and 51 ppt of  $^{238}\text{U}$  and  $^{232}\text{Th}$ , respectively. The outer dimensions of the box are 152 cm (L)  $\times$  142 cm (W)  $\times$  142 cm (H). The wall thickness is 3 cm and the total mass is 6.4 tons. It is made of oxygen-free copper (OFC). A 1 cm-thick acrylic container for the liquid scintillator is nested inside of the copper box.

### 3.4 Liquid scintillator

A variety of backgrounds produced by radiogenic particles from components in and near the NaI(Tl) crystals, including the crystal PMT-originating and the NaI(Tl) internal backgrounds, are efficiently rejected by an anticoincidence requirement with PMT signals from the liquid scintillator (LS) and neighboring crystal signals. This innermost active and passive shielding is provided by 2200 L of Linear Alkyl-Benzene (LAB)-based LS contained in the acrylic box. The inner walls of the acrylic container and the outer surfaces of the crystal assemblies are wrapped with specular reflective films<sup>3</sup> to increase the LS light collection efficiency. The LS-produced photons are detected by eighteen 5-inch Hamamatsu PMTs (R877) that are attached to the two sides of the box. The minimum distance between the crystal PMTs and the copper-box inner wall is approximately 40 cm, as indicated in Fig. 1.

Through  $\alpha$ -particle measurements discussed in Sect. 5, we determined upper limits for the intrinsic  $^{238}\text{U}$  and  $^{232}\text{Th}$  contaminations in the LAB-LS of 7 and 4 ppt, respectively.

The top 9 cm of the acrylic box holding the LS was left unfilled as a safety margin in the event of a temperature increase that might cause an expansion of the LS volume. To maintain a high LS light output by preventing contact with oxygen and water, gas boil-off from a liquid nitrogen dewar is supplied to this space at a rate of 3 liters per minute and the humidity at the top of the liquid is maintained at

<sup>2</sup> The steel has  $^{238}\text{U}$  and  $^{232}\text{Th}$  contamination levels that were measured with the Y2L HPGe setup to be 40 and 100 ppt, respectively.

<sup>3</sup> 3M Vikuiti-ESR film.

**Table 1** Measured radioactivity levels in the COSINE-100 crystals. The light yield is measured at 59.6 keV with a  $^{241}\text{Am}$  source and checked for consistency with the 46.5 keV internal  $^{210}\text{Pb}$   $\gamma$ -ray peak. The unitsfor light yield are photoelectrons per keV (PEs/keV). Chain equilibrium is assumed for the  $^{238}\text{U}$  and  $^{232}\text{Th}$  values

| Crystal   | Mass (kg) | Size (inches diameter $\times$ length) | Powder   | $\alpha$ Rate (mBq/kg) | $^{40}\text{K}$ (ppb) | $^{238}\text{U}$ (ppt) | $^{232}\text{Th}$ (ppt) | Light yield (PEs/keV) |
|-----------|-----------|--|----------|------------------------|-----------------------|------------------------|-------------------------|-----------------------|
| Crystal-1 | 8.3       | 5.0 $\times$ 7.0                       | AS-B     | 3.20 $\pm$ 0.08        | 34.7 $\pm$ 4.7        | < 0.02                 | 1.3 $\pm$ 0.4           | 14.9 $\pm$ 1.5        |
| Crystal-2 | 9.2       | 4.2 $\times$ 11.0                      | AS-C     | 2.06 $\pm$ 0.06        | 60.6 $\pm$ 4.7        | < 0.12                 | < 0.6                   | 14.6 $\pm$ 1.5        |
| Crystal-3 | 9.2       | 4.2 $\times$ 11.0                      | AS-WSII  | 0.76 $\pm$ 0.02        | 34.3 $\pm$ 3.1        | < 0.04                 | 0.4 $\pm$ 0.2           | 15.5 $\pm$ 1.6        |
| Crystal-4 | 18.0      | 5.0 $\times$ 15.3                      | AS-WSII  | 0.74 $\pm$ 0.02        | 33.3 $\pm$ 3.5        |                        | < 0.3                   | 14.9 $\pm$ 1.5        |
| Crystal-5 | 18.3      | 5.0 $\times$ 15.5                      | AS-C     | 2.06 $\pm$ 0.05        | 82.3 $\pm$ 5.5        |                        | 2.4 $\pm$ 0.3           | 7.3 $\pm$ 0.7         |
| Crystal-6 | 12.5      | 4.8 $\times$ 11.8                      | AS-WSIII | 1.52 $\pm$ 0.04        | 16.8 $\pm$ 2.5        | < 0.02                 | 0.6 $\pm$ 0.2           | 14.6 $\pm$ 1.5        |
| Crystal-7 | 12.5      | 4.8 $\times$ 11.8                      | AS-WSIII | 1.54 $\pm$ 0.04        | 18.7 $\pm$ 2.8        |                        | < 0.6                   | 14.0 $\pm$ 1.4        |
| Crystal-8 | 18.3      | 5.0 $\times$ 15.5                      | AS-C     | 2.05 $\pm$ 0.05        | 54.3 $\pm$ 3.8        |                        | < 1.4                   | 3.5 $\pm$ 0.3         |
| DAMA      |           |  |          | < 0.5                  | < 20                  | 0.7–10                 | 0.5–7.5                 | 5.5–7.5               |

< 2.0%. The scintillating liquid volume and its relatively high heat capacity helps keep the temperature of the liquid and crystals stable at  $(24.20 \pm 0.05)^\circ\text{C}$ .

## 4 NaI(Tl) crystal detectors

### 4.1 Crystal assembly

The COSINE-100 experiment uses low-background NaI(Tl) crystals (labeled Crystal-1 to Crystal-8, or C1–C8) that were developed in cooperation with Alpha Spectra Inc. (AS). The eight NaI(Tl) crystals were grown out of batches of powders with successive improvements, with AS-B and AS-C: Alpha Spectra purified powders, AS-WSII: Alpha Spectra WIMPSint-II grade powder and AS-WSIII: Alpha Spectra WIMPSint-III grade powder. The final crystals are cylindrically shaped and hermetically encased in OFC tubes (1.5 mm thick) with quartz windows attached at each end. Each crystal's lateral surfaces were wrapped in roughly 10 layers of 250  $\mu\text{m}$ -thick PTFE reflective sheets and then inserted into the OFC tubes in a nitrogen gas environment and sealed to make them gas tight. A 12.0 mm-thick quartz window is light-coupled to each end of the crystal via 1.5 mm thick optical pads.<sup>4</sup> These, in turn, are light-coupled to 3-inch Hamamatsu R12669SEL PMTs via a small amount of high viscosity optical gel.<sup>5</sup> The average quantum efficiency of the PMTs is 35%. The copper cylinders that encapsulate the crystals have 16 mm-diameter calibration windows with either a reduced copper thickness of 0.5 or a 0.13 mm-thin Mylar cover to facilitate low energy source calibrations.

Four different powder grades were used to grow the eight crystals (see Table 1). Although AS does not release the

specifics of each powder for proprietary reasons, results from our detailed studies of these powders and crystals are described in Refs. [27,36].

### 4.2 Calibration system and crystal array geometry

The performance levels of the crystals and the liquid scintillator are monitored with a variety of calibration sources; four different  $\gamma$ -ray sources including  $^{241}\text{Am}$ ,  $^{57}\text{Co}$ ,  $^{137}\text{Cs}$  and  $^{60}\text{Co}$  are used for the energy calibration. Four stainless steel tubes with a 9.5 mm outer-diameter and 2.5 mm thickness penetrate the copper and acrylic boxes and pass through the liquid scintillator. Access to the calibration tube requires the dismantling of two of the plastic scintillators and the removal of eight of the lead castle bricks. During calibration campaigns, needle-type source tips encapsulated in a stainless steel rod are inserted into the tube. In this way, calibrations can be done without opening the front shield.

The eight NaI(Tl) crystals are arranged in a  $4 \times 2$  array that is supported by a two-layer acrylic table located in the central region of the liquid scintillator. The crystals are oriented such that their calibration windows directly face the nearest calibration tube. Two external source calibrations were performed on September 22, 2016 and on December 27, 2016 so far. The crystal arrangement and numbering scheme are shown in Fig. 3.

### 4.3 Background activity of the crystals

Before the installation of the crystals in the COSINE shield, background event rates from internal radioactive contaminants in the NaI(Tl) crystals were measured in the KIMS-CsI setup at A6 [27,36]. After the insertion of the crystals into the shield and prior to filling the liquid scintillator container, their background levels were remeasured to verify that they were free of any additional contamination. Over-

<sup>4</sup> Eljen Technology EJ-560.

<sup>5</sup> Eljen Technology EJ-550.

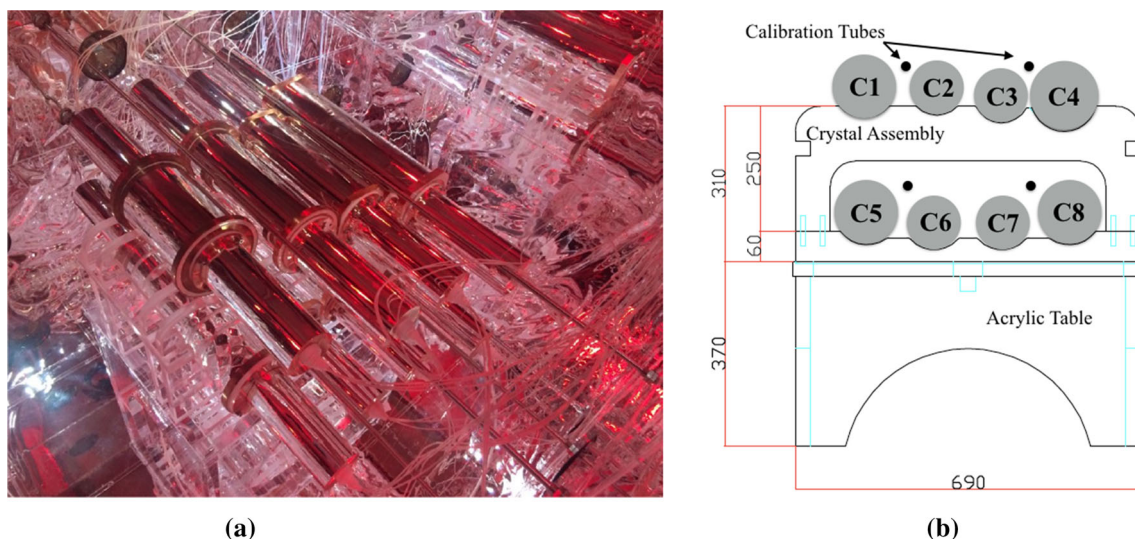


**Fig. 3** The  $4 \times 2$  NaI(Tl) crystal array. Each crystal has two, 3-inch PMTs and is encapsulated in a thin Polytetrafluoroethylene (PTFE) reflector and copper casing. The crystal arrangement is shown in (a) and a diagram of the crystal arrangement is shown in (b). An acrylic

table supports the crystal assemblies. The eight crystals are labeled C1 through C8 and the locations of the four calibration holes are indicated. The table dimensions are indicated in mm and viewed from the A-side of the detector

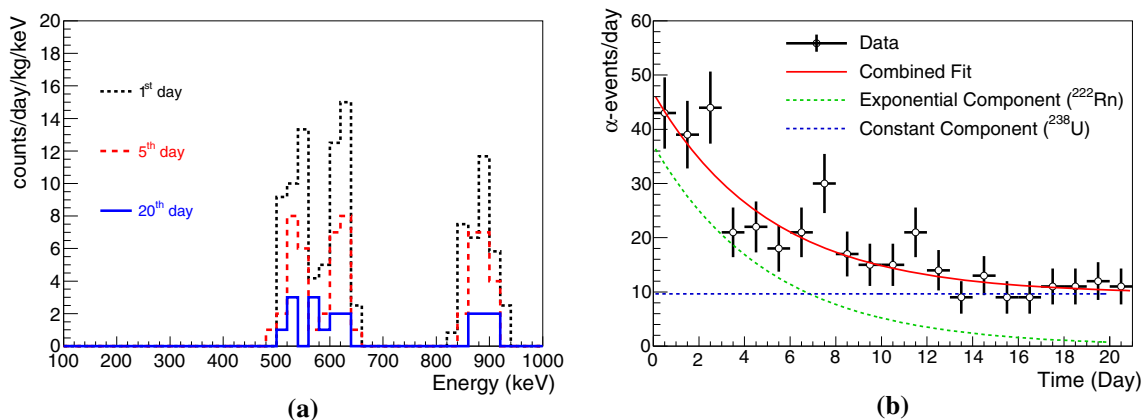


**Fig. 4** **a** Energy spectra of  $\alpha$ -particles originating from the 70 mL PTFE cell at different times. The histogram labeled “1st day” is when the 70 mL cell was first assembled while that labeled 20th day is 19 days later. The  $\alpha$ -induced events are selected based on pulse shape discrimination criteria. **b** The number of measured  $\alpha$ -events as a function

of time. A fit with an exponential plus a flat component was performed with the assumption that decreasing components originate from external contamination of  $^{222}\text{Rn}$  and from its daughter particle decays, while the flat component is produced by long lived isotopes in the  $^{238}\text{U}$  chain that are intrinsic to the LS

all, the eight crystals have high light yields and acceptable  $^{238}\text{U}$  and  $^{232}\text{Th}$  contaminations (see Table 1). The light yield of Crystal-5 and Crystal-8, however, decreased over the first few weeks and their optical coupling is suspected to have degraded.

The  $^{210}\text{Pb}$  levels were improved by a factor of two between the AS-C and AS-WSII powders, and  $^{40}\text{K}$  levels also improved by a factor of two between the WS-II and WS-III powders. The powder grade closely correlates with the contamination level of the grown crystals, as demonstrated by

the  $^{40}\text{K}$  levels, which vary strongly according to the powder type; within each specific batch of powder, the  $^{40}\text{K}$  radioactivity levels are consistently reproduced. The  $^{210}\text{Po}$  (in equilibrium with  $^{210}\text{Pb}$ ) levels, as determined from the  $\alpha$  particle rates, are higher than those achieved by DAMA [9]; the origin of this elevated rate is not yet fully understood. Some of the  $^{210}\text{Pb}$  may originate from lead or radon that is introduced into the raw materials prior to crystallization. Chain equilibrium is assumed for the interpretation of  $^{238}\text{U}$  and  $^{232}\text{Th}$  related radioactivity measurements, with the exception of  $^{210}\text{Pb}$ .

## 5 Liquid scintillator veto system

The LAB-LS contains a few percent of 2,5-diphenyloxazole (PPO) as the fluor and for wavelength shifting, with a trace amount of p-bis-(o-methylstyryl)-benzene (bis-MSB) to serve as a second wavelength shifter [43]. To produce the final 2200 L LAB-LS volume, a 110 L concentrated solution of PPO and bis-MSB was first prepared. This master solution was then mixed with LAB in a 1:20 ratio to make the final LAB-based LS. The LS was produced in a surface-level laboratory and moved to the A5 tunnel at Y2L immediately after production. The LS was passed through two layers of 0.1  $\mu\text{m}$  pore-size filters while being transferred into the acrylic container.

Since PPO may have a relatively high level of contamination by radioisotopes, a water extraction method [44] with 17 M $\Omega$  deionized water was used to extract impurities from the master solution. To remove the residual water after this treatment, a high flux ( $\sim 30$  L/min) of  $\text{N}_2$  gas was bubbled through the liquid until the exhaust-gas humidity level reached  $\sim 20$  ppm  $\text{H}_2\text{O}$ .

Internal  $\alpha$ -contamination measurements of the LAB-based LS were carried out with a 70 mL PTFE cell detector. Figure 4 shows the results of these background measurements. Signals induced by  $\alpha$  particles are separated from  $\gamma$ -induced events by means of pulse shape discrimination. The observed  $\alpha$ -energy spectrum is understood as  $^{222}\text{Rn}$  contamination that might have occurred during the assembly of the small-cell detector. As can be seen in Fig. 4, the  $\alpha$ -peaks decreased at a rate that is consistent with the 3.8 day half life of  $^{222}\text{Rn}$ . A simulation of  $^{210}\text{Pb}$  shows that the remaining  $^{210}\text{Pb}$  in LS does not contribute a significant observable background in the crystals. Because we only observe  $\alpha$ -events corresponding to  $^{222}\text{Rn}$ , the level of the intrinsic  $^{238}\text{U}$  chain activity in the LAB-LS was determined to be 7 ppt from a fit to the time dependence with a flat component in addition to an exponential with a 3.8 day half life. An upper limit for an intrinsic  $^{232}\text{Th}$  chain activity was measured to be 4 ppt using a time difference analysis of consecutive  $\alpha$ -decays [36]. Measurements with a prototype LS detector and simulation studies show that these upper limits are sufficiently small to ensure negligible background contributions to the NaI(Tl) crystal energy spectra [45].

Energy calibrations of the LS veto system are performed with various  $\gamma$ -ray sources inserted in the calibration tubes. The position dependence of the light yields was inferred from measurements made with disk sources placed at different positions on the outside of the LS container during the commissioning period. After applying these LS characteristics to data, the LS deposited energy spectrum shown in Fig. 5 is obtained.

Coincident events between the LS and a single crystal show a time correlation for LS signals with energies above

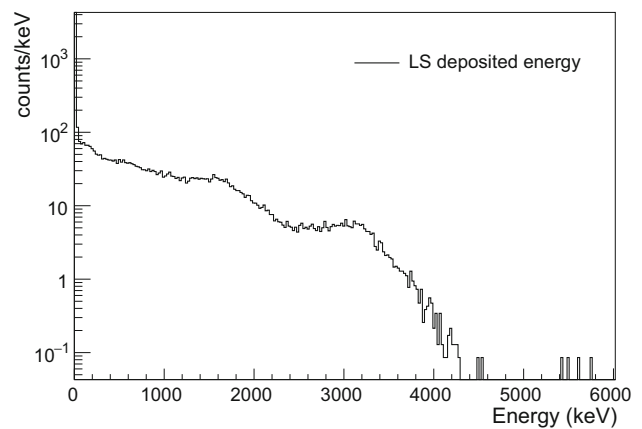


**Fig. 5** The LS energy spectrum for initial 16.7 days of data. The signals from all 18 readout PMTs are summed. Note that the LS PMTs are not included in the event trigger. Only passive data that occur during a time window that includes the crystal trigger time are recorded

20 keV. With a 20 keV LS energy threshold requirement and a 200 ns coincidence window between LS and crystal signals, there are only 0.3% accidental coincidences in the sample of the selected events. With these conditions, the energy spectrum of events in Crystal-1 that occur in coincidence with LS signals is shown in Fig. 6. By comparing the crystal energy spectrum with and without the coincidence condition in the 2–4 keV region, we can determine a 72% tagging efficiency for 3 keV emissions from  $^{40}\text{K}$  decay. Similarly, Crystal-2 has a tagging efficiency of 74%. Both agree well with simulated efficiencies and the measured  $^{40}\text{K}$  activities from the previous measurements in the KIMS array. For other crystals, this data-driven efficiency estimation is difficult due to additional 3 keV events from cosmogenically produced  $^{109}\text{Cd}$ , low light yields or low internal  $^{40}\text{K}$  levels. For these crystals, tagging efficiencies from simulations are between 65 and 75%, depending on the crystal's location in the array.

## 6 Muon detector system

It is known that the cosmic-ray muon intensity is modulated by seasonal temperature variations of the atmosphere [42, 46, 47]. Thus, signals in COSINE-100 that are induced by cosmic-ray muons could mimic dark matter annual modulation signals. To tag cosmic-ray muons and study their correlations with crystal signals, we have surrounded the COSINE-100 detector with 37 muon detectors made from panels of 3 cm thick plastic scintillator. The scintillation panels are read out by 2-inch Hamamatsu H7195 PMTs via acrylic light guides.

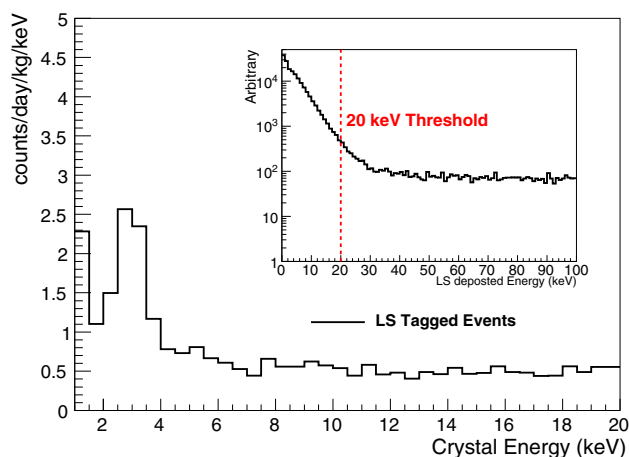


**Fig. 6** The spectrum of Crystal-1 signals that occur in coincidence with LS signals with  $E > 20$  keV is shown. The 3 keV  $^{40}\text{K}$  events are tagged in the LS system with a 72% efficiency

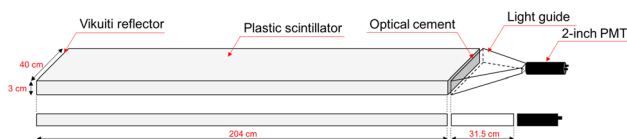


**Fig. 7** A schematic view of a muon detector

### 6.1 Muon detector panels

The muon detector system is made of scintillating plastic from Eljen Technology, EJ-200. This material provides favorable properties, such as high light output (10,000 photons/MeV), PMT friendly wavelengths (efficiency peaks at 425 nm) and a long optical attenuation length (380 cm).

Prior to attaching the PMTs, each scintillator was polished and wrapped with white reflective sheets, a layer of aluminum foil, and a black sheet, an arrangement that was found to provide efficient light collection, create a barrier against external light leaking into the scintillator, and protect against physical damage to the plastic. Epoxy<sup>6</sup> is used to make the optical connection between the plastic scintillator and the light guide, and between the light guide and the PMT photocathode. For the 2 m long panels that are coupled to only one PMT, a specular reflecting sheet is attached to the edge of the scintillator that is opposite of the PMT. This improves the light output by about 8%. The 3 m long panels are coupled to a PMT at each end and form the top surface of the main shield. The arrangement of the COSINE-100 muon detection panels in the shielding structure is shown in Fig. 1. A schematic diagram of a single panel is shown in Fig. 7; a production photo is shown in Fig. 8.

<sup>6</sup> Saint Gobain, BC-600.

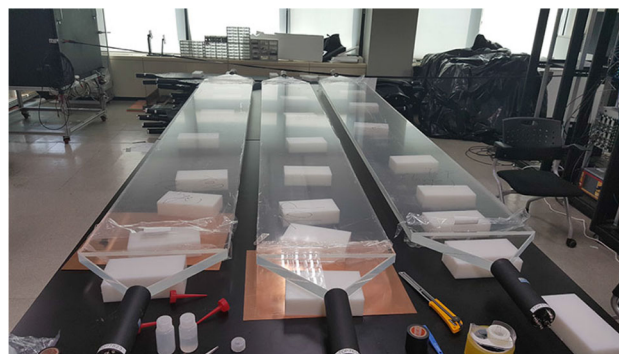


**Fig. 8** A photo of the muon detector production

### 6.2 Performance of the plastic scintillator

We performed various tests on the panels in a surface-level laboratory where the cosmic-ray muon flux is high. For these tests, a small-size muon panel placed above the muon detector under study provided a trigger signal. This arrangement was used to determine the light yield and its dependence on the distance to the PMT. To select muon candidates, we required a coincidence between the trigger panel and the panel being tested. With a moderate threshold requirement, cosmic-ray muon candidates were selected and their charge spectrum was fitted to a Landau function. The most probable value from the fit results was subsequently used to calibrate the charge spectrum of a single panel as well as to align the panel-to-panel spectra.

To understand the performance and efficiency of each muon detector panel, we stacked them four at a time and triggered on coincidences between pairs of counters. By comparing the responses of one pair in events triggered by the other pair, we inferred the panel efficiencies for cosmic-ray muons to be 99.5%; the 0.5% loss could be attributed to horizontal muons that strike the edge of one panel and minor misalignments of the panels.

The muon detection panels were subsequently installed underground in the COSINE-100 shielding structure at Y2L. Figure 9 shows the total charge distribution from one of the top panels where muon-like events are well separated from low-energy  $\gamma$ -ray-induced backgrounds.

The cosmic-ray muon flux at the COSINE-100 detector was measured to be  $328 \pm 1$  (stat.)  $\pm 10$  (syst.) muons/m<sup>2</sup>/day [37]. The current NaI(Tl) crystal event selection requires a coincidence within a 30 ms time window between a crystal triggered event and a muon panel event to select the muon induced events. A further refinement of this condition and studies of those selected events for their time dependence are actively on-going.



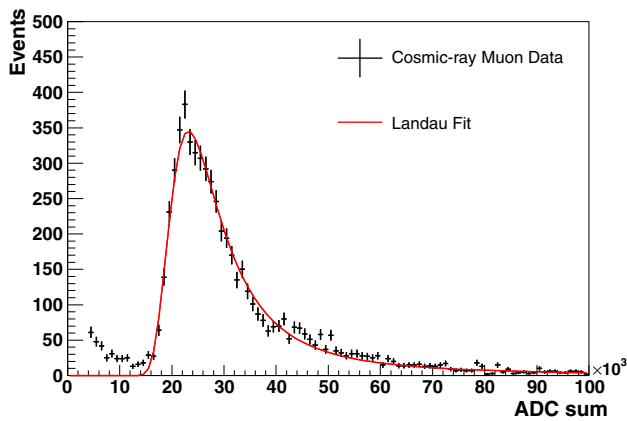


**Fig. 9** The summed charge spectrum of muon-like events in one of the top-side panels for 48.3 days of initial data in the COSINE-100 detector. The solid curve is the result of a fit to the spectrum with a Landau function. Events with ADC sum below 14,000 counts are primarily due to  $\gamma$ -ray-induced events

## 7 Electronics and data acquisition system

### 7.1 Electronics and data flow

The data acquisition system is located inside the detector room in order to minimize the signal attenuation through cables and to reduce environmental effects. The system consists of DAQ modules, HV supply modules, and computers. All electronics and their AC power are controlled by a dedicated computer in the control room adjacent to the detector room. Figure 10 shows an overall data-flow diagram for the COSINE-100 experiment.

There are 16 3-inch crystal-readout PMTs, 18 5-inch PMTs for the LS system and 42 2-inch PMTs for the muon system. Since each crystal PMT has two readout channels, there are a total of 92 signal channels that are read out and recorded by the DAQ system. In addition, there are a total of 76 separate high voltages that have to be supplied and monitored.

Signals from each crystal PMT are amplified by custom-made preamplifiers: the high-gain anode signal by a factor of 30 and the low-gain signal from the 5th stage dynode by a factor of 100. Figure 11 shows the PMT voltage divider diagram where the anode and 5th dynode readout circuits are indicated. The amplified signals are digitized by 500 MSPS (megasamples per second), 12 bit flash analog-to-digital converters (FADCs). Both the low-gain dynode and high-gain anode waveforms are recorded whenever an anode signal produces a trigger. The dynode signals do not generate triggers. The high-gain signals have linear responses for energies up to about 100 keV while the dynode signals start to show non-linear responses above about 3,000 keV.

Signals from the liquid scintillator PMTs are amplified by a gain of 30 and are digitized in a charge-sensitive 62.5 MSPS

ADC (SADC). Unamplified signals from the muon panels are directly connected to SADCs. The SADC returns the integrated charge and the time of the input signals. Triggers from individual channels are generated by field programmable gate arrays (FPGAs) embedded in the FADCs and SADCs. The final trigger decision for an event is made by a trigger and clock board (TCB) that also synchronizes the timing of the different channels.

For channels with waveforms that are only non-triggered baselines, the contents are suppressed to zero. Raw data are converted to a ROOT format [48] in the DAQ computer and automatically transferred daily to CPU farms at the Institute for Basic Science and Yale University where further processing is performed. The total trigger rate during a physics run is 28 Hz, of which crystal FADC triggers constitute 15 Hz and muon SADC triggers contribute the remaining 13 Hz. The total anticipated data size is 7 TB per year. In addition, a fraction of the real-time raw-data waveforms are sent to an online server for monitoring purposes and hour-by-hour monitoring variables are produced shortly after the raw data creation.

### 7.2 DAQ for LS and muon veto

The LS veto and the muon detector PMTs (60 channels in total) are connected to three SADC modules. We use a 192 ns integration time to contain the plastic and liquid scintillator signals, both of which have decay times less than 10 ns [49].

The SADC modules can produce their own triggers and event records. For this case, the SADC trigger signals are based on the integrated charge. For the muon counters, 4000 ADC-count thresholds (integrated charge approximately 763 pC) are used to reject PMT noise and  $\gamma$ -ray induced backgrounds. Since the observed charges for muon events are typically larger than 12,000 ADC counts, this trigger-threshold does not reject any muon candidates. SADC triggers are generated when at least two channels exceed the threshold within a 400 ns time window, since any muon that traverses the detector should produce hits in at least two panels. In addition, a separate trigger is generated if one of the LS PMTs registers a signal (with  $> 4000$  integrated ADC counts) in coincidence with one of the muon panels, corresponding to events where cosmic-ray muons traverse, or stop inside the LS volume. There are no triggers that are based only on LS PMT signals. When the SADC modules produce a trigger, the TCB does not send a trigger signal to the FADC modules; if there is no accompanying FADC trigger, only data from the three SADC modules are recorded. Otherwise, the SADC channels provide passive data that are recorded when FADC triggers are generated by the TCB.

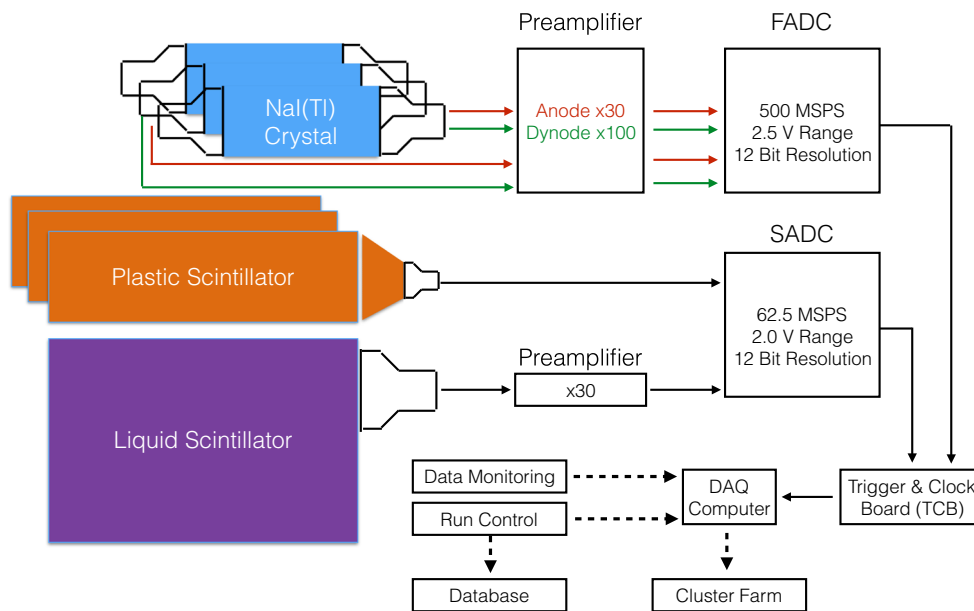


**Fig. 10** Data flow block diagram. The crystal signals are recorded with FADCs while the plastic and liquid scintillator signals are recorded with SADCs. Global triggers are formed at the TCB board

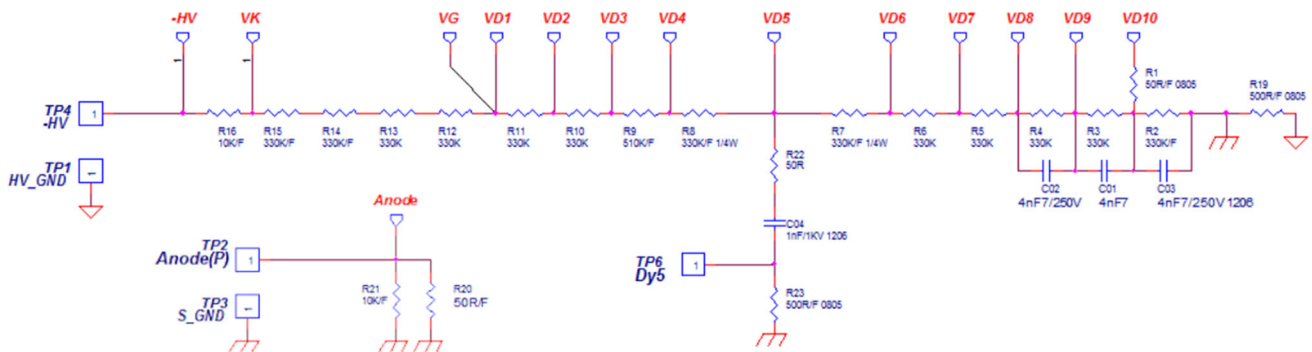


**Fig. 11** Schematic of crystal PMT voltage divider

### 7.3 Crystal DAQ

The NaI(Tl) crystal waveforms are digitized by FADCs. Each FADC module contains four channels and eight FADC modules are used in COSINE-100. Their range is from 0 to 2.5 V with 12-bit resolution. Similarly to the SADC, the trigger configuration parameters are uploaded into FPGAs located in each FADC module.

The trigger is generated by high-gain anode signals. The trigger condition for a NaI(Tl) crystal is satisfied when the signal crosses a height equivalent to one photoelectron in both PMTs coupled to a single crystal within a 200ns time window. A “hit” is defined as a single photoelectron (SPE) with 10 or more ADC counts (greater than 6mV) while a typical SPE signal in the COSINE-100 detector is greater than 25 ADC counts. The SPE height spectrum is shown in Fig. 12. If at least one crystal satisfies the trigger condition, the TCB transmits trigger signals to all of the FADCs

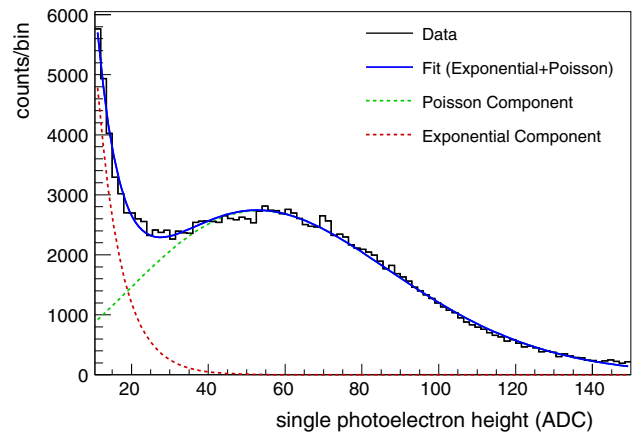


**Fig. 12** The SPE height spectrum for one of two PMTs in Crystal-1 and SADCs. All of the crystal, LS, and muon-detector PMT signal data are stored for FADC triggers. For each FADC channel, this corresponds to an 8 μs-long waveform starting

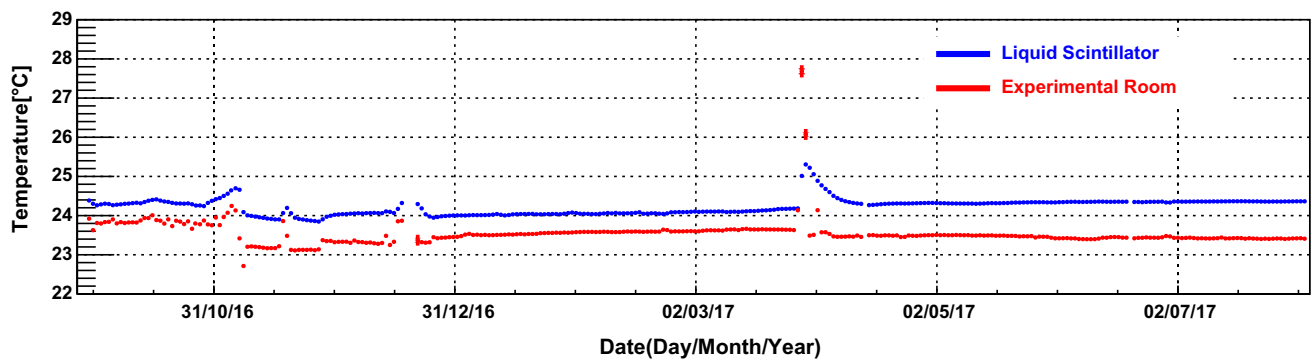


**Fig. 13** Temperature measurements as a function of time in 1 year period. The temperature of the liquid scintillator in the vicinity of Crystal-2 and one of the detector room temperatures are displayed.

Note that the offset between the two measurements is due to different sensor calibrations and the high rise in the temperature on March 29, 2017 was due to a sudden air conditioner failure

approximately  $2.4 \mu\text{s}$  before the time of the first hit. For each SADC channel this corresponds to the maximum integrated charge within a  $4 \mu\text{s}$  search window and to the associated time of that maximum.

## 8 Slow monitoring system

For stable data-taking and systematic analyses of seasonal variations, it is important to control and continuously monitor environmental parameters such as detector temperatures, high voltage variations, humidities, etc. For this, we employ a variety of sensors for specific monitoring tasks. These devices are controlled and read out by a common database server and a visualization program. In this section, we briefly describe the environmental monitoring system for the COSINE-100 experiment.

We monitor temperatures at various locations using an 8-channel data logger coupled to K-type thermocouple sensors. Three of the sensors are placed in contact with the liquid scintillator inside the copper box. The others monitor the room and tunnel temperatures.

High voltages are provided and controlled by a CAEN HV crate that is monitored with software provided by the company. All of the supplied HVs, currents, and PMT statuses are monitored once per minute. We use three analog sensors to measure the relative humidity. The humidity sensors are connected to the slow-monitoring server via a commercial DAQ module. The same DAQ module is used to monitor output voltages from the preamplifier system. The detector-room oxygen level is monitored with a device that has an RS-232 port for serial communication. As a safety measure the  $\text{O}_2$ -level is prominently displayed in the detector room. The recorded air-conditioner data include the status of the equipment, the room temperature and humidity, and various alarms that are transmitted via an RS-485 that is used for

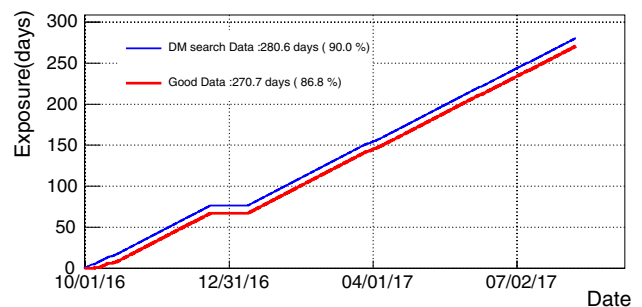


**Fig. 14** COSINE-100 exposure versus date. The detector stably collects physics data with a 90% live time, of which 96% is high-quality. Short instabilities at the beginning of the physics data-taking are mainly due to temperature fluctuations in the vicinity of the crystals and DAQ tests. The data taking was interrupted on December 20, 2016 for a 2-week long calibration campaign with external radioactive sources

continuous monitoring. All of the monitoring equipment are powered by a 80kVA uninterruptible power supply (UPS) that contains a network-based monitoring module that provides various protocols. The slow monitoring system checks the UPS status and input/output voltages every 5 s. A commercial RAD7 radon-level monitor samples the air atmosphere in the detector room and records the radon level every 30 min. We use InfluxDB<sup>7</sup> for storing the slow monitoring data and Grafana<sup>8</sup> for visualization of data. Figure 13 shows one of the slow monitoring data panels.

## 9 Initial performance of the COSINE-100 detector

After the completion of the detector component installation, we performed a series of calibrations and began a physics run. The experiment has been operating stably and collecting

<sup>7</sup> <https://www.influxdata.com>.

<sup>8</sup> <https://grafana.com>.

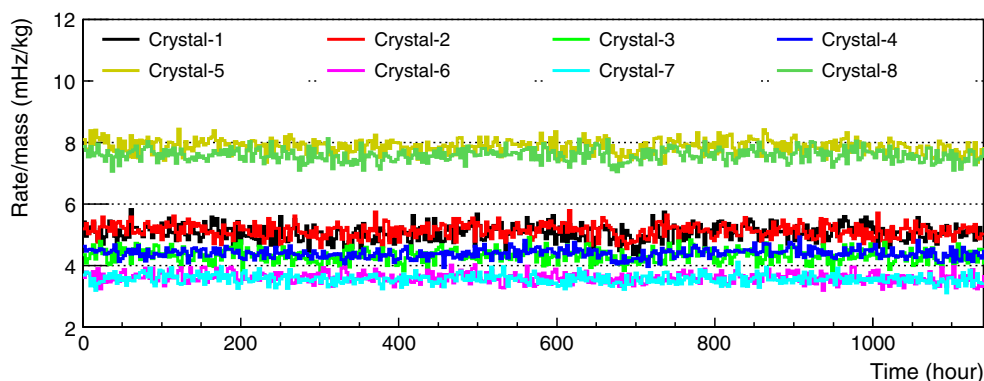


**Fig. 15** Crystal trigger rates versus time (in h) for the first physics run (48 days). All of the crystals show stable behavior throughout this running period and the rest of data-taking

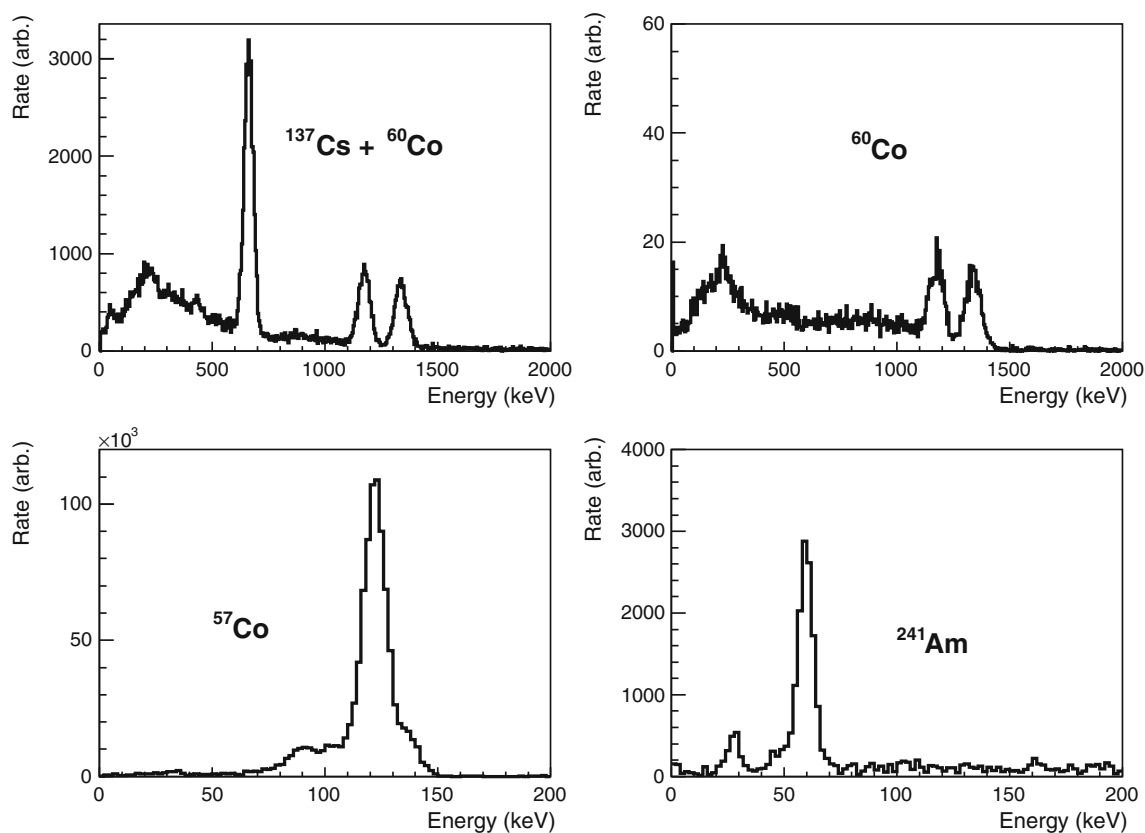


**Fig. 16** The measured calibration energy spectrum in Crystal-6 for  $^{60}\text{Co}$  and  $^{137}\text{Cs}$ ,  $^{60}\text{Co}$  only,  $^{241}\text{Am}$  and  $^{57}\text{Co}$  calibration sources (clockwise from top left)

physics-quality data since late September 2016 (see Figs. 14, 15). Monitoring shifts are performed to check data quality in every two hours using automatically generated physics distributions and plots from the slow monitoring system. Data are defined as a good quality if all DAQ systems are operational with no missing signals, the LS temperature is not higher than  $25^\circ\text{C}$ , and the total trigger rate is not higher than 100 Hz for more than 10 min. In this section, we discuss detector calibrations and evaluations of the initial performance.

### 9.1 Energy calibration

The main goal of the external radioactive source energy calibration campaign was to determine the light characteristics of the crystals and the scintillating liquid, including light yields, energy scales, and energy resolutions. The calibration stability is monitored during data-taking periods by tracking internal  $\beta$ - and  $\gamma$ -ray peaks from radioactive contaminants in the crystals.

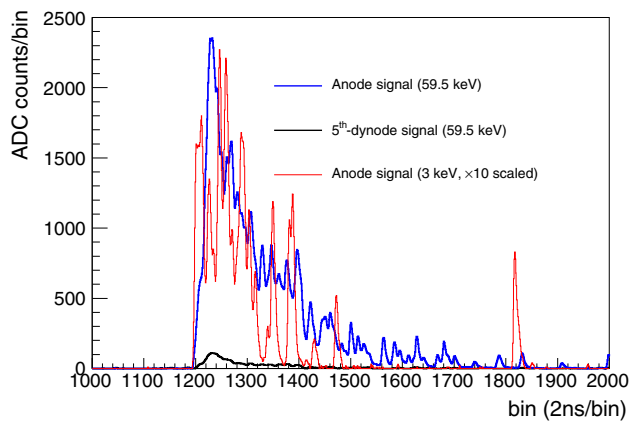


**Fig. 17** Crystal-1 raw waveforms from a 59.5 keV  $^{241}\text{Am}$  source and 3 keV  $^{40}\text{K}$  emission (scaled up by a factor of ten) are overlaid for anode signal comparisons. For high and low gain comparison, the dynode readout of the same 59.5 keV signal is also included

At energies above a few hundred keV, calibrations are made using  $\gamma$ -ray lines from  $^{137}\text{Cs}$  and  $^{60}\text{Co}$  sources;  $^{137}\text{Cs}$  produces a mono-energetic  $\gamma$ -ray peak at 662 keV while  $^{60}\text{Co}$  produces peaks at 1173 and 1332 keV. For energies below 150 keV,  $^{241}\text{Am}$  and  $^{57}\text{Co}$  radioisotopes with peaks at 59.5 and 122 keV, respectively, are used.

Energy spectra measured with these sources in place are shown in Fig. 16. The five dominant peaks from the above-mentioned sources, as well as internal radioisotope peaks, are used to set the energy scale of the crystal spectra based on linear fits. These energy scales are set separately for the anode readout and the dynode readout.

For the low-energy region, the high-gain anode signal waveforms are used. The energy scale is set by the 59.5 keV  $^{241}\text{Am}$  calibration peak. This peak is also used to determine the energy resolution and evaluate the crystal light yield. Additional continuous checks of the energy scale are provided by the 46.5 keV  $^{210}\text{Pb}$   $\gamma$ -ray line and the 3 keV  $^{40}\text{K}$  emission line from internal contaminants. From the first three months data analysis, the  $^{210}\text{Pb}$  peak positions for the 16 PMTs were measured to be shifted on average by  $(0.6 \pm 0.3)\%$  relative to the beginning. The measured energy resolution, defined as the standard deviation divided by the energy from a Gaussian fit, is 5% at 59.5 keV in the Crystal-1 anode readout. Representative anode waveforms for 59.5 and 3 keV signals, and the dynode waveform for the same 59.5 keV signal, are shown in Fig. 17.

We characterize the PMT responses to SPEs using a sample of isolated hits occurring in the tails of anode signal waveforms. This information is used to determine the light yields observed in each PMT and, from that, each crystal. These spectra and light yields are monitored on a regular basis in order to monitor the stability level of each PMT. Figure 12 shows the SPE height spectrum of one of the PMTs in Crystal-1. A combined fit of a Poisson function to represent

the SPE response plus an exponential to represent a baseline noise component is shown. Results from this fit are used to infer the average number of SPEs in 59.5 keV  $^{241}\text{Am}$   $\gamma$ -ray signals. With the exception of C5 and C8, the light yields of the COSINE-100 crystals are twice as high as those of the DAMA crystals [9]; the light yields are listed in Table 1.

## 9.2 Low energy noise rejection

Because the hardware trigger threshold is set low, the DAQ system collects a large number of non-physics events that are primarily caused by PMT noise that is coincident between the two PMTs coupled to different ends of the same crystal. These coincident noise events could be due to radioactivity in the PMT glass and/or circuitry, the discharge of accumulated space charge in one of the PMTs, PMT dark current, after-pulses of large pulses, etc. Since PMT-generated noise signals are concentrated at low energy regions where they could potentially mimic dark matter signals, these noise events have to be rejected by software selection criteria.

The DAMA group reported signal selection criteria based on time-integrated charge fractions that efficiently distinguish PMT noise waveforms from those generated by scintillation events in NaI(Tl) crystals. The selection exploits the characteristic short decay times of PMT noise pulses.

DAMA defines the integrated charge in the  $[0, 50\text{ ns}]$  time range normalized by the total charge (integrated over  $[0, 600\text{ ns}]$ ) as X2 (the fast charge), and that integrated over  $[100, 600\text{ ns}]$  time range normalized by the same total charge as X1 (slow charge) [9, 50]. A two-dimensional plot of X1 versus X2 for low energy COSINE-100 noise and  $\beta$ -/ $\gamma$ -ray induced signal events is shown in Fig. 18, where signal events populate the high-X1 and low-X2 region while PMT noise events concentrate in the complementary and well-separated, high-X2 and low-X1 region. Crystal-specific selection requirements on X1 and X2 typically reject 80% of the PMT-generated noise events above 2 keV while retaining 99% of the tagged Compton scattering events at 2 keV using  $^{60}\text{Co}$  calibration data.

Although a large fraction of PMT-noise events are removed by this X1:X2 cut, some PMT noise-like events still remain. Therefore, we developed further analysis cuts to remove these events. One is based on the charge asymmetry between the signal in the two PMTs coupled to the same crystal, defined as

$$\text{Asymmetry} = \frac{Q1 - Q2}{Q1 + Q2},$$

where Q1 and Q2 are the total charges measured by each of the two PMTs. In the asymmetry distribution shown in Fig. 19, the X1:X2 requirement has already been applied. Many events with apparent energy below 3 keV have asymmetries that are larger than those for true signal events that

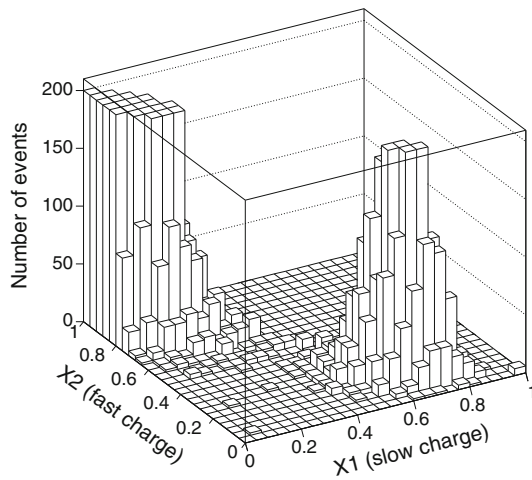


**Fig. 18** A two-dimensional plot of the fast and slow charge fractions for Crystal-1. PMT noise events populate the high X2 and low X1 region while signal events have low values of X2 and high values of X1

occur near one or the other end of the crystal, suggesting that these events are caused by visible light produced near one of the PMTs. Asymmetric events of this type are only weakly correlated with the X1:X2 requirement, which exploits the pulse development in time. To suppress these events, we require that the absolute value of the asymmetry parameter be smaller than 0.5. The combined efficiency estimated using the  $^{60}\text{Co}$  events at 2 keV with the X1:X2 and asymmetry selections is measured to be 98%, while rejecting 90% of the PMT noise events.

Some noise pulses evade the X1:X2 cut and the asymmetry cut. These contain merged pulse clusters that correspond to an anomalously large number of SPEs. These are removed

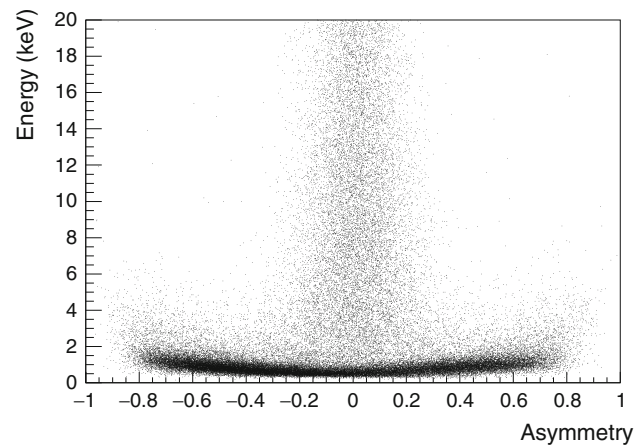


**Fig. 19** Energy versus asymmetry for Crystal-1 (see text for the definition of asymmetry). Further noise event reduction is accomplished by a selection criteria based on the asymmetry of the total charges measured by the two PMTs. The middle vertical band centered near zero is predominantly due to  $\beta$ - $\gamma$ -ray-induced events inside the crystal, while the highly asymmetric events with energies below a few keV are due to events that are likely of PMT origin

by placing a limit on the average number of SPEs per cluster. For example, we demand that a signal event should contain roughly 2 SPEs or less per cluster at 2 keV. This requirement is applied after the X1:X2 and asymmetry selection conditions and the total efficiency of all three selections for the  $^{60}\text{Co}$  events at 2 keV is better than 95%, while the total PMT noise rejection is 95%. The low energy spectrum after the application of the three selection requirements is shown in Fig. 20. Studies of other noise suppression parameters and the development of a multivariate technique to optimize selections based on these are in progress.

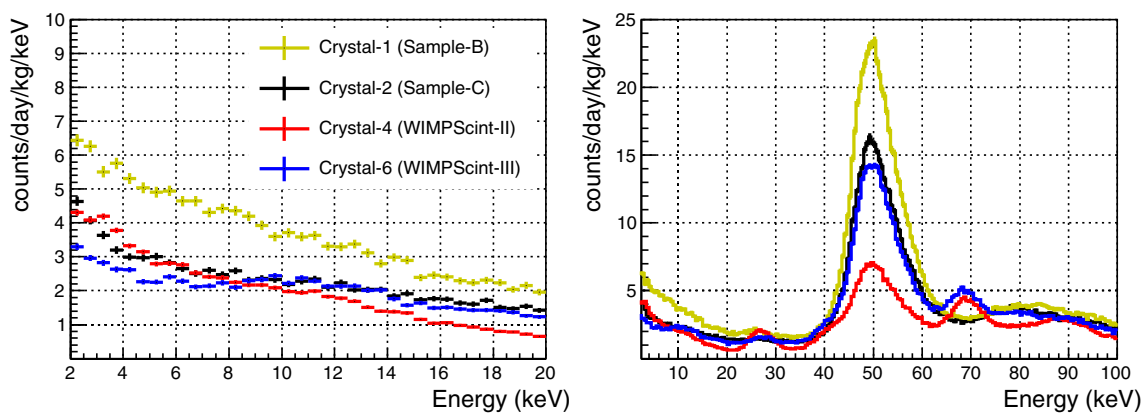


**Fig. 20** Energy spectrum comparisons for four crystals from different powder samples. (left) A zoomed view of the  $E \leq 20$  keV region of the spectrum. The background levels are lowest for Crystal-4 and Crystal-6, which reflect their lower  $^{210}\text{Pb}$  and  $^{40}\text{K}$  contamination levels. The spectra were made after the application of the three noise rejection criteria. (right) The peak near 50 keV reflects the  $^{210}\text{Pb}$  contamination level in

each crystal. Crystal-4 and Crystal-6 have been underground for less than 1 year and so cosmogenic peaks (e.g.  $^{125}\text{I}$  at 67.8 keV) are additionally seen. These spectra are obtained using 59.5 days of the initial data. We have estimated efficiencies at 2 keV better than 95% using  $^{60}\text{Co}$  Compton calibration data. Therefore, efficiency corrections are not applied

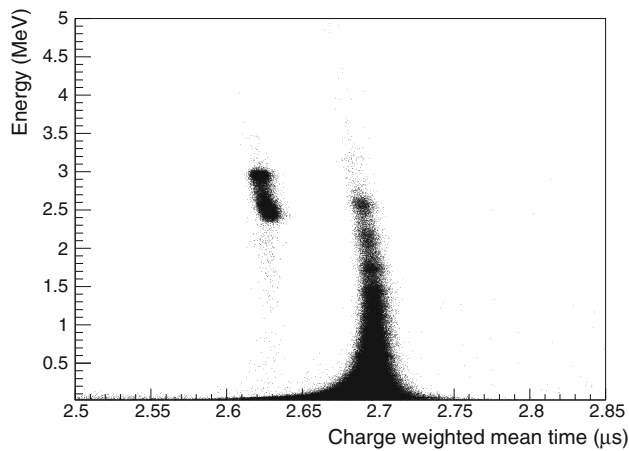


**Fig. 21** Charge-weighted mean time (horizontal) versus energy (vertical) for Crystal-6. The island of events with low mean time and high energies is due to  $\alpha$ -induced events and is well separated from  $\beta$ -/ $\gamma$ -ray-induced events. Due to quenching effects, the measured  $\alpha$ -energy is lower than its full energy

### 9.3 $\alpha$ activity and $^{210}\text{Po}$ background

Separation of  $\alpha$ - from  $\beta$ -/ $\gamma$ -ray- induced events is achieved by using the charge-weighted mean-time pulse shape discrimination method [36]. The island of events in the Fig. 21 scatter plot of charge-weighted mean-time of a signal waveform versus its total energy is due to  $\alpha$ -events, and is well separated from  $\beta$ -/ $\gamma$ -ray-induced events.

The  $^{238}\text{U}$  and  $^{232}\text{Th}$  contamination levels measured by  $\alpha$  –  $\alpha$  and  $\beta$  –  $\alpha$  time correlation methods [36] in the eight crystals are too low to account for the total observed  $\alpha$ -rates. This suggests that the bulk of the  $\alpha$ -rate is due to decays of  $^{210}\text{Po}$  ( $E_\alpha = 5.3$  MeV) nuclei that originate from  $\beta$ -decays of  $^{210}\text{Pb}$  nuclides in the crystals that occurred sometime during the powder and/or crystal processing stages [27, 36]. The  $\alpha$ -rate for each crystal is listed in Table 1.

### 9.4 $^{40}\text{K}$ background

Events generated by decays of  $^{40}\text{K}$  contaminants in the crystals are identified by coincidence signals between a 3 keV emission in one NaI(Tl) detector and a 1460 keV  $\gamma$ -ray in one of the other NaI(Tl) crystals or an energy deposition in the LS. Figure 22 shows a scatter plot of the energy in Crystal-2 versus that in other NaI(Tl) crystals for these multi-hit coincidence events. The  $^{40}\text{K}$  signal forms the island of events near 3 keV in the Crystal-2 signal and near 1460 keV in the other NaI(Tl) crystal. The  $^{40}\text{K}$  background level in each crystal is determined by comparing the measured coincidence rate with a GEANT4-simulated efficiency using the method described in Ref. [36].

The source of  $^{40}\text{K}$  in the NaI(Tl) crystals is almost entirely from contamination that originated in the NaI powder, and no

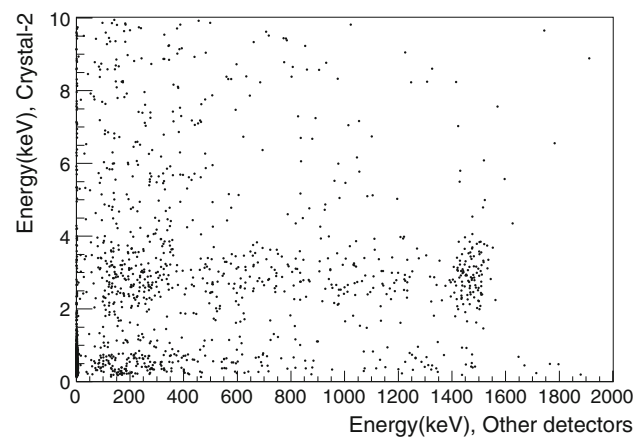


**Fig. 22** A scatter plot of energy deposition in Crystal-2 (vertical) versus that deposited in other crystals in the array (horizontal). The  $^{40}\text{K}$  events are identified as the distinct island in the energy spectrum near 3 keV in Crystal-2 and 1460 keV measured in the one of the other crystals

significant increase in the contamination level is introduced during the crystal growing procedure [27, 36]. The  $^{\text{nat}}\text{K}$  measurements for all crystals are listed in Table 1, following the latest analysis with improved statistics. The  $^{\text{nat}}\text{K}$  content in the DAMA crystals is in the 10–20 ppb range [9], levels that have been achieved in some of the most recently produced COSINE-100 crystals.

### 9.5 Background summary

The high-energy  $\gamma$ -ray spectra show pronounced background peaks: a 1460 keV line from  $^{40}\text{K}$  and lines from daughter nuclei in the  $^{238}\text{U}$  and  $^{232}\text{Th}$  decay chains. These background levels are reduced by as much as 80% by requiring single-hit crystal events with no signal in the LS. Using a GEANT4 simulation, we estimate the efficiency for vetoing these background components as a function of the crystal's position in the detector array. Figure 23 shows a comparison between the high-energy spectrum with and without the LS veto application from real data.

Figure 20 shows a comparison of background levels in Crystal-1, Crystal-2, Crystal-4 and Crystal-6. The  $^{210}\text{Pb}$  contamination level was reduced by a factor of four in Crystal-4 as compared to that in Crystal-1, reflecting improvements in the powder. Additionally, we are able to achieve a background level close to 2 counts/day/keV/kg at 6 keV. The  $^{210}\text{Pb}$  contamination level in Crystal-6 is lower than in Crystal-1 but higher than that in Crystal-4. The lower background level in the Crystal-6 energies below 8 keV and the flatter distribution between 2–20 keV compared to Crystal-4 indicate that this crystal contains less surface  $^{210}\text{Pb}$  contamination relative to that for bulk  $^{210}\text{Pb}$ . The  $^{40}\text{K}$  level in Crystal-6 is 17 ppb, which is the lowest of the four crystals. The spectrum of

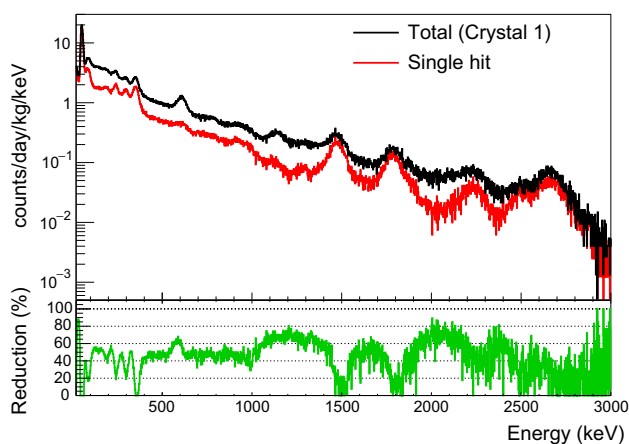


**Fig. 23** A comparison of the Crystal-1 energy spectrum before (black line) and after (red line) application of the LS veto. The  $\gamma$ -ray radiation from daughter nuclei of the  $^{238}\text{U}$  and  $^{232}\text{Th}$  decay chains in the external shielding materials are reduced significantly by the LS veto requirement. The lower panel shows a reduction in percentage as a function of the energy

Crystal-7 shows similar characteristics and background levels as those of Crystal-6 since they are created with the same geometry at the same time from the same ingot. The Crystal-3 spectrum shows a similar shape as Crystal-4 because they are made from the same type of powder. Crystal-5 and Crystal-8 show about 10 counts/day/keV/kg at 2 keV due to their low light yields and relatively higher background contamination. The main contributors to the remaining background below 6 keV are  $^{210}\text{Pb}$   $\beta$ -decay events,  $^{40}\text{K}$  emissions, and cosmogenic activations of I/Te,  $^{22}\text{Na}$ ,  $^{109}\text{Cd}$ , and  $^3\text{H}$ . The cosmogenically activated backgrounds will diminish significantly after a few years deep underground at Y2L. Analysis tools aimed at lowering the energy threshold are under development.

## 9.6 Nuclear recoil calibration

To characterize the scintillation properties of nuclear recoils, a study on neutron-induced nuclear recoils is ongoing in a specially prepared neutron calibration facility based on a D–D fusion device that produces 2.42 MeV mono-energetic neutrons. Nuclear recoil events are collected for small crystal targets (2 cm  $\times$  2 cm  $\times$  1.5 cm) made from each of the crystal ingots placed in the neutron beam. The neutron scattering angle is used to infer the energy of the recoil nucleus in the target crystal after selecting on the time-of-flight between the NaI(Tl) crystal signal and the neutron detector signal. From this calibration, an event selection efficiency for low energy nuclear recoil events near the threshold region is determined.

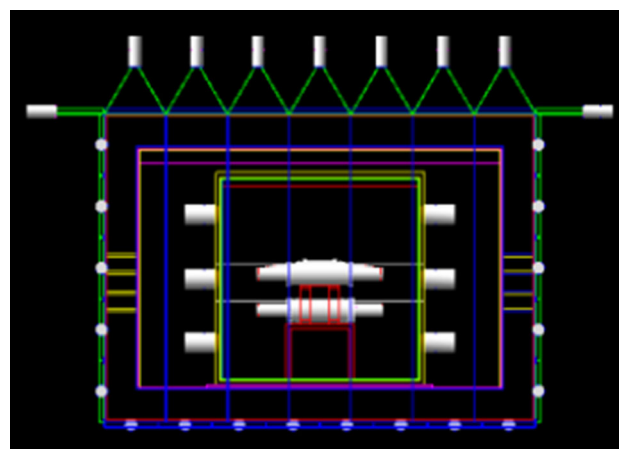


**Fig. 24** A schematic view of the detector geometry. The copper encapsulation is shown in white in the middle, the acrylic crystal support structure is shown in red, the copper box is shown in yellow, the lead castle is shown in red, and the muon panels are shown in blue

## 10 Background model and detector simulations

To understand the NaI(Tl) crystal backgrounds and determine WIMP detection efficiencies for the COSINE-100 experiment, we have performed Monte-Carlo simulations of the detector and its environment using the GEANT4 package [51]. The simulation uses the geometry of the COSINE-100 experiment as shown in Fig. 24.

### 10.1 Background modeling

To measure the reduction efficiency of the  $^{40}\text{K}$  3 keV background provided by tagging the accompanying 1460 keV  $\gamma$ -ray in one of the other NaI(Tl) crystals or the LS, and to compare this to the efficiency provided by the other crystals alone, we generated  $^{40}\text{K}$  decays at random locations inside a NaI(Tl) crystal for the cases with and without an LS veto. From these simulations, we determined the Crystal-6 tagging efficiency by other crystals without LS is  $31.7 \pm 0.1\%$  and by the LS only is  $64.9 \pm 0.2\%$ . The total combined efficiency is  $81.7 \pm 0.3\%$ . The efficiency is measured in the crystal energy range between 2 and 6 keV by requiring the LS energy deposit be larger than 20 keV. Efficiencies vary depending on the crystal location in the detector. For example, Crystal-1 (at the corner of the array) shows higher coverage by the LS (75%) than neighboring crystals (17%), but the combined efficiency is similar to that of Crystal-6 (82%). The tagging efficiency of the 1460 keV  $\gamma$ -ray in the LS-only case is lower because the range of the  $\gamma$ -ray in the NaI(Tl) crystal is shorter than in the LS. Therefore, more  $\gamma$ -rays are stopped in the other crystals than in the LS. These estimated efficiencies are in agreement with measurements.

Backgrounds from remnants of cosmogenic activation of I and Te radioisotopes still persist but are declining with



lifetimes that are less than 100 days. We also observe external backgrounds from the PMTs, shielding materials, and  $^{222}\text{Rn}$  in the air. External backgrounds are expected to be mostly tagged by the LS veto. Thus, the low energy COSINE-100 detector backgrounds are predominantly from internal sources, especially  $^{210}\text{Pb}$ , of which the main contributions are from crystal bulk contamination intrinsic to the raw material, and from  $^{222}\text{Rn}$  exposure during crystal growing and handling procedures. More detailed information on the background understanding of the NaI(Tl) crystal can be found in Ref. [29].

## 10.2 Detector response and trigger simulation

To understand the detector response, we are currently developing a full detector simulation that allows us to analyze simulated data using the same framework as real data. The simulation includes photon generation, photoelectron conversion, amplification, and FADC digitization.

The simulation of the scintillation decay time distributions for the NaI(Tl) crystal signals for electron and nuclear recoils was based on signals generated by a  $^{241}\text{Am}$  source and tuned to the data. The simulated time distribution of photons detected in the PMTs exhibit a 247 ns decay time that is in a good agreement with the known value of 250 ns [49]. We will use digitized simulated waveforms and a trigger logic simulation to determine the trigger efficiency and, ultimately, perform a detailed simulation of WIMP-induced signals.

## 11 Sensitivity of the COSINE-100 experiment

The primary goal of COSINE-100 is to directly confirm or reject the hypothesis that the annual modulation observed by DAMA is due to dark matter. Here, we present the projected sensitivity of the COSINE-100 experiment compared with the DAMA-allowed signal regions as interpreted by Ref. [52].

We assume the standard halo model of dark matter [8] and calculate theoretical modulation amplitudes of spin-independent WIMP-nucleon interactions in a NaI(Tl) detector as functions of recoil energy. We further assume an average Earth velocity of 250 km/s and that WIMPs obey a Maxwellian velocity distribution, with  $v_0 = 220$  km/s,  $v_{esc} = 650$  km/s, and  $\rho_0 = 0.3$  GeV/cm<sup>3</sup>. To directly compare our results with the modulation amplitudes observed by DAMA, we assume quenching factors of 0.3 for sodium and 0.09 for iodine, as reported by DAMA [9]. These theoretical modulation rates are computed for WIMP masses between 1 and  $10^3$  GeV/c<sup>2</sup> and cross sections between  $10^{-43}$  and  $10^{-37}$  cm<sup>2</sup>.

Using this theoretical model, we identify regions in the WIMP phase space compatible with DAMA's observed mod-

ulation signal. The modulation amplitudes obtained from theory are compared with the modulation amplitude as a function of energy observed by DAMA [11] using a binned likelihood analysis between 1 and 20 keV [53]. As can be seen in Fig. 25, two DAMA-allowed regions have been identified, with the low-mass region corresponding to WIMP-Na scatters and the high-mass region corresponding to WIMP-I scatters. Additionally, a  $\chi^2$  analysis is performed on these data that gives results that are consistent with the likelihood analysis.

We also make use of an ensemble of Monte Carlo experiments combined with this theoretical model to establish the projected sensitivity of the COSINE-100 detector in the case of no observed WIMP signal. For this analysis, we investigate the sensitivity that will be achieved after 2 years of data taking, giving a total exposure of 212 kg year. A flat representative background of 4.3 counts/day/kg/keV with no modulation or decay components is assumed based on the currently achieved background levels of the detector. The flat mean background is calculated by weighting individual crystal masses in the spectrum between 2 and 20 keV. We simulate the experiment within the background-only hypothesis by generating histograms of the expected event rate that fluctuate with Poisson statistics about the 4.3 counts/day/kg/keV backgrounds for nuclear recoils of various energies. These histograms are binned in one-day intervals. We then fit a cosine function to the simulated data with a fixed period of 1 year and a phase of June 2<sup>nd</sup>. The fit result is then used to determine the modulation amplitude observed by COSINE-100 for nuclear recoil energies ranging from 1 to 20 keV. These simulated amplitudes are compared to the theoretically predicted modulation amplitudes for various WIMP masses and cross sections. In total, 200 iterations of the COSINE-100 experiment are simulated to obtain 90% C.L.,  $3\sigma$ , and  $5\sigma$  exclusion limits. The results of the likelihood analysis are shown in Fig. 25. We also present the projected detector sensitivity for the energy range of 2–20 keV.

As can be seen in Fig. 25, for the 1 keV threshold case, the median projected sensitivity of COSINE-100 will be able to exclude the low-mass DAMA-allowed region to a significance of nearly  $5\sigma$  at a 90% C.L. and a majority of the high-mass DAMA-allowed region at a 90% C.L., assuming no WIMP-nucleon-scattering-like modulation is observed.

## 12 Summary and conclusions

The main goal of the COSINE-100 experiment is to independently confirm or dispute DAMA's long-standing annual modulation signature. The detector is comprised of eight ultra-low background NaI(Tl) crystals encapsulated in copper and shielded by several layers of external radioactivity

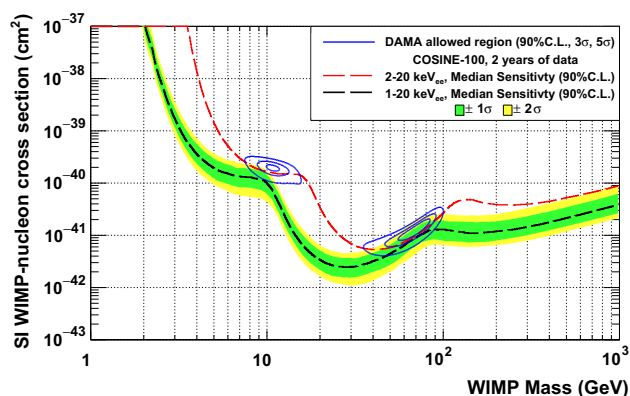


**Fig. 25** Projected upper limits on the spin-independent WIMP-nucleon cross section using a likelihood analysis. The black curve represents the median exclusion limit of COSINE-100 assuming a 1 keV threshold at a 90% C.L. The green and yellow regions represent  $1\sigma$  and  $2\sigma$  deviations from this median, respectively. The blue contours designate DAMA-allowed regions for spin-independent interactions. A more conservative exclusion limit assuming a 2 keV threshold for COSINE-100 is shown in red

attenuators. Unlike the DAMA apparatus, the experiment is additionally equipped with cosmic-ray muon panels and a liquid scintillator veto to tag  $^{40}\text{K}$ -induced events and those that may originate from non-WIMP-induced interactions external to the crystal. The detector has been taking data since September 30, 2016, and the fraction of physics-quality data is greater than 95%. A variety of control and monitoring systems are in place that collect and record environmental data that are used in correlation studies with the crystal data. The initial data performance levels are consistent with expectations and we expect to continue stable data-taking for the next 2 years. With these data, a model-independent analysis will be performed to prove or refute DAMA while we can also examine a large portion of the WIMP-mass/cross-section parameter regions that are favored by the DAMA results.

**Acknowledgements** We thank the Korea Hydro and Nuclear Power (KHNP) Company for providing underground laboratory space at Yangyang. This work is supported by: the Institute for Basic Science (IBS) under project code IBS-R016-A1, Republic of Korea; UIUC campus research board, the Alfred P. Sloan Foundation Fellowship, NSF Grants no. PHY-1151795, PHY-1457995, DGE-1122492 and DGE-1256259, WIPAC, the Wisconsin Alumni Research Foundation, Yale University and DOE/NNSA Grant no. DE-FC52-08NA28752, United States; STFC Grant ST/N000277/1 and ST/K001337/1, United Kingdom; and CNPq and Grant no. 2017/02952-0 FAPESP, Brazil.

**Open Access** This article is distributed under the terms of the Creative Commons Attribution 4.0 International License (<http://creativecommons.org/licenses/by/4.0/>), which permits unrestricted use, distribution, and reproduction in any medium, provided you give appropriate credit to the original author(s) and the source, provide a link to the Creative Commons license, and indicate if changes were made. Funded by SCOAP<sup>3</sup>.

## References

- D. Huterer, *Gen. Relativ. Gravit.* **42**, 2177 (2010)
- D. Clowe et al., *Astrophys. J.* **648**, L109 (2006)
- P.A.R. Ade et al. (Planck Collaboration), *Astron. Astrophys.* **594**, A13 (2016)
- B.W. Lee, S. Weinberg, *Phys. Rev. Lett.* **39**, 165 (1977)
- G. Jungman, M. Kamionkowski, K. Griest, *Phys. Rep.* **267**, 195 (1996)
- M.W. Goodman, E. Witten, *Phys. Rev. D* **31**, 3059 (1985)
- A.K. Drukier, K. Freese, D.N. Spergel, *Phys. Rev. D* **33**, 3495 (1986)
- K. Freese, M. Lisanti, C. Savage, *Rev. Mod. Phys.* **85**, 1561 (2013)
- R. Bernabei et al. (DAMA Collaboration), *Nucl. Instrum. Methods A* **592**, 297 (2008)
- R. Bernabei et al. (DAMA Collaboration), *Phys. Lett. B* **480**, 23 (2000)
- R. Bernabei et al. (DAMA Collaboration), *Eur. Phys. J. C* **73**, 2648 (2013)
- D. Nygren, Unpublished (2011). [arXiv:1102.0815](https://arxiv.org/abs/1102.0815)
- C. Savage, K. Freese, P. Gondolo, *Phys. Rev. D* **74**, 043531 (2006)
- J. Kopp, V. Niro, T. Schwetz, J. Zupan, *Phys. Rev. D* **80**, 083502 (2009)
- J.P. Ralston, Unpublished (2010). [arXiv:1006.5255](https://arxiv.org/abs/1006.5255)
- D.S. Akerib et al. (LUX Collaboration), *Phys. Rev. Lett.* **118**, 021303 (2017)
- A. Tan et al. (PandaX Collaboration), *Phys. Rev. Lett.* **117**, 121303 (2016)
- X. Cui et al. (PandaX Collaboration), *Phys. Rev. Lett.* **119**, 181302 (2017)
- E. Aprile et al. (XENON Collaboration), *Phys. Rev. Lett.* **109**, 181301 (2012)
- E. Aprile et al. (XENON Collaboration), *Phys. Rev. Lett.* **119**, 181301 (2017)
- R. Agnese et al. (SuperCDMS Collaboration), *Phys. Rev. Lett.* **112**, 041302 (2014)
- R. Agnese et al. (SuperCDMS Collaboration), *Phys. Rev. Lett.* **116**, 071301 (2016)
- R. Agnese et al. (SuperCDMS Collaboration), *Phys. Rev. Lett.* **112**, 241302 (2014)
- S.C. Kim et al. (KIMS Collaboration), *Phys. Rev. Lett.* **108**, 181301 (2012)
- K. Abe et al. (XMASS Collaboration), *Phys. Lett. B* **759**, 272 (2016)
- E. Aprile et al. (XENON Collaboration), *Phys. Rev. Lett.* **118**, 101101 (2017)
- P. Adhikari et al. (KIMS Collaboration), *Eur. Phys. J. C* **76**, 185 (2016)
- J. Amare et al. (ANAIS Collaboration), *Eur. Phys. J. C* **76**, 429 (2016)
- G. Adhikari et al. (KIMS Collaboration), *Eur. Phys. J. C* **77**, 437 (2017)
- J. Amare et al. (ANAIS Collaboration), *Nucl. Instrum. Methods A* **742**, 187 (2014)
- J. Amare et al. (ANAIS Collaboration), *J. Phys. Conf. Ser.* **718**, 042052 (2016)
- J. Cherwinka et al. (DM-Ice Collaboration), *Phys. Rev. D* **90**, 092005 (2014)
- E. Barbosa de Souza et al. (DM-Ice Collaboration), *Phys. Rev. D* **95**, 032006 (2017)
- K. Fushimi et al., *J. Phys. Conf. Ser.* **718**, 042022 (2016)
- J. Xu, F. Calaprice, F. Froberg, E. Shields, B. Suerfu, *AIP Conf. Proc.* **1672**, 040001 (2015)
- K.W. Kim et al. (KIMS Collaboration), *Astropart. Phys.* **62**, 249 (2015)

37. H. Prihtiadi et al. (COSINE-100 Collaboration), (2017). [arXiv:1712.02011](https://arxiv.org/abs/1712.02011)
38. J.J. Zhu et al. (KIMS Collaboration), High Energy Phys. Nucl. **29**, 8 (2005)
39. M.J. Lee et al. (KIMS Collaboration), J. Korean Phys. Soc. **57**, 713 (2011)
40. H.S. Lee et al. (KIMS Collaboration), Nucl. Instrum. Methods A **571**, 644 (2007)
41. H.S. Lee et al. (KIMS Collaboration), Phys. Lett. B **633**, 201 (2006)
42. J. Cherwinka et al. (DM-Ice Collaboration), Phys. Rev. D **93**, 042001 (2016)
43. J.S. Park et al. (RENO Collaboration), Nucl. Instrum. Methods A **707**, 1016 (2013)
44. M. Yeh, Nucl. Instrum. Methods A **578**, 329 (2007)
45. J.S. Park et al. (KIMS Collaboration), Nucl. Instrum. Methods A **851**, 103 (2017)
46. G. Bellini et al. (DAMA Collaboration), JCAP **05**, 015 (2012)
47. P. Desiati, T.K. Gaisser, Phys. Rev. Lett. **105**, 121102 (2010)
48. R. Brun, F. Rademakers, Nucl. Instrum. Methods A **389**, 81 (1997)
49. G.F. Knoll, *Radiation detection and measurement* (Wiley, New York, 2010)
50. R. Bernabei et al. (DAMA Collaboration), JINST **7**, P03009 (2012)
51. S. Agostinelli et al., Nucl. Instrum. Methods A **506**, 250 (2003)
52. C. Savage et al., JCAP **04**, 010 (2009)
53. W.G. Thompson (COSINE-100 Collaboration), in *Proceedings 15th International Conference on Topics in Astroparticle and Underground Physics (TAUP 2017) Sudbury, Ontario, Canada, July 24–28, 2017*. [arXiv:1711.01488](https://arxiv.org/abs/1711.01488)